A Model-Based 3D Multi-slice Helical CT Reconstruction Algorithm for Transportation Security Application

Pengchong Jin*, Eri Haneda*, Charles A. Bouman*, Ken D. Sauer †

*School of Electrical and Computer Engineering, Purdue University, West Lafayette, IN 47907-0501
†Department of Electrical Engineering, University of Notre Dame, 275 Fitzpatrick, Notre Dame, IN 46556-5637

Abstract—**Multi-slice helical CT is widely used for baggage inspection in transportation security due to its fast acquisition speed and large scan coverage. In addition, recent studies indicate that model-based reconstruction has the potential to improve image quality and reduce artifacts relative to traditional filtered backprojection (FBP) method. In this paper, we present the results of a 3D model-based reconstruction algorithm on a multi-slice helical scan of actual baggage with high and low density objects, acquired on a medical CT system. We compared our reconstruction results to conventional FBP reconstructions and illustrated the potential value of our algorithm in terms of image quality and artifact reduction.**

I. INTRODUCTION

Computed tomography (CT) is widely used in transportation security applications [1], [2]. Among various CT scanner geometries, multi-slice helical CT has come into wide use due to its fast acquisition and large scan coverage. In fact, many airports have installed multi-slice helical CT systems as a central component of baggage screening. However, the more complex geometry of multi-slice helical CT also poses challenges in reconstruction. For example, as cone angles become wider, there is an increasing need to use true 3D reconstruction methods in order to avoid the image artifacts introduced by 2D approximations.

Moreover, the task in transportation security is quite different from the medical problem. In the medical application, it is critical to preserve fine details of soft tissue structure; however, in the security application, typically it is more important to obtain precise estimates of object boundary and its average density. Also, in security, the objects typically have densities that are substantially greater than water.

Recently, model-based reconstruction (MBR) algorithms have been shown to be effective in the reconstruction of multislice helical scan CT data [3]. These algorithms have the advantage that they can incorporate more detailed models of both the scanner and the objects being reconstructed. In addition, they offer flexibility in the application of transportation security since they allow for more accurate reconstruction for nontraditional geometries, such as with limited view data [4]. Model-based algorithms have the potential to more accurately account for a wide array of scanner characteristics including

photon counting and electronic noise, beam hardening, metal attenuation and scatter, and the detector point-spread function. More accurate modeling of the scanner can be used to reduce streaking artifacts from high density objects, which arise in many CT applications. In addition, the MBR method incorporates a prior model that can be tuned to the characteristics of typical objects and the performance metrics of interest.

In this paper, we apply the methods of 3D model-based reconstruction (MBR) to the problem of transportation security imaging. Our approach is based on maximum a posterior (MAP) reconstruction along with the iterative coordinate descent (ICD) optimization method. We also describe how our algorithm can be parallelized on multicore processing hardware.

In our results, we present 3D MBR cross-sections from real multislice helical scan data of travel bags packed with a variety of high and low density objects, imaged on a medical scanner. Our results indicate that MBR has the potential to produce reconstructions with fewer artifacts than analytic reconstruction methods.

II. STATISTICAL MODEL FOR IMAGE RECONSTRUCTION

Let $x \in \mathbb{R}^M$ be the image vector, and let $y \in \mathbb{R}^N$ be the vector of projection measurements. We assume x and y are related by a linear sparse matrix operator A,

$$y = Ax \tag{1}$$

The matrix coefficient A_{ij} reflects the formation of i-th projection by j-th voxel.

In the Bayesian statistical framework, both x and y are considered as random, and the reconstruction is most commonly computed as the maximum a posterior (MAP) estimate given by

$$\hat{x} = \arg \min_{x \geq 0} \left\{ -\log p(y|x) - \log p(x) \right\} \tag{2}$$

where $p(y|x)$ is the likelihood term corresponding to the forward projection model and $p(x)$ is the prior distribution of x. Also notice that we impose a positivity constraint on the image.

Given the image x, the received photon count λ_i of the i-th projection follows a Poisson distribution with mean $\lambda_{T,i} e^{-A_{i*}x}$ where $\lambda_{T,i}$ is the photon count of the i-th projection obtained in an air calibration scan. The line integral

of i-th projection can then be obtained by $y_i = \log\left(\frac{\lambda_{T,i}}{\lambda_i}\right)$. Using the second order Taylor expansion, the log likelihood term can be approximated by a quadratic function [5],

$$\log p(y|x) \approx -\frac{1}{2}(y - Ax)^T D(y - Ax) + c(y) \qquad (3)$$

where D is the diagonal matrix with diagonal elements $D_{i,i}$ which are proportional to the photon counts λ_i, and $c(y)$ is a term depending only on y. Notice that in this case, a smaller value of λ_i indicates that the associate projection is less heavily weighted.

The prior distribution $p(x)$ incorporates knowledge about the object being reconstructed, x. We will describe the prior model in detail in the next section.

III. METHOD AND ALGORITHM

A. 3D Forward Projection Model

To calculate the projection matrix A, we use the distance-driven (DD) model [6]. Figure 1 illustrates how the 3D projection geometry is decomposed into the z axis that falls along the object's translation direction, and the xy-plane, which is perpendicular to z [3]. Each voxel is flattened along the dimension most parallel to the detector, and the coefficient A_{ij} is calculated as the product of xy-plane projection, B_{ij}, and z-direction projection, C_{ij}.

$$A_{ij} = B_{ij} \times C_{ij} \qquad (4)$$

The coefficients B_{ij} and C_{ij} are calculated as the convolution of the detector response and the flattened voxel profile to yield

$$B_{ij} = \frac{\Delta_{xy}}{\Delta d_c \cos\tilde{\theta}} clip\left[0, \frac{W_c + \Delta d_c}{2} - |\delta_c|, \min(W_c, \Delta d_c)\right] \qquad (5)$$

$$C_{ij} = \frac{1}{\Delta d_r \cos\phi} clip\left[0, \frac{W_r + \Delta d_r}{2} - |\delta_r|, \min(W_r, \Delta d_r)\right] \qquad (6)$$

where W denotes the voxel's width when projected onto the detector, Δd denotes the detector width, subscript c and r denote channel and row respectively, θ and ϕ are the ray angles in xy-plane and z-direction, and $\tilde{\theta}$ is the adjusted ray angle defined by

$$\tilde{\theta} = \left(\theta + \frac{\pi}{4}\right) \ mod \ \frac{\pi}{2} - \frac{\pi}{4} \ . \qquad (7)$$

The function $clip$ is defined by $clip[a, b, c] = \min(\max(a, b), c)$.

B. Prior Model

We model the image x as a Markov random field, with a 26-point 3D neighborhood and the following distribution

$$p(x) = \frac{1}{z}\exp\left\{-\sum_{\{s,r\}\in\mathcal{C}} b_{s,r}\rho(x_s - x_r)\right\} \qquad (8)$$

where ρ is the positive and symmetric potential function and $\mathcal{C}$ is the set of all pairwise cliques.
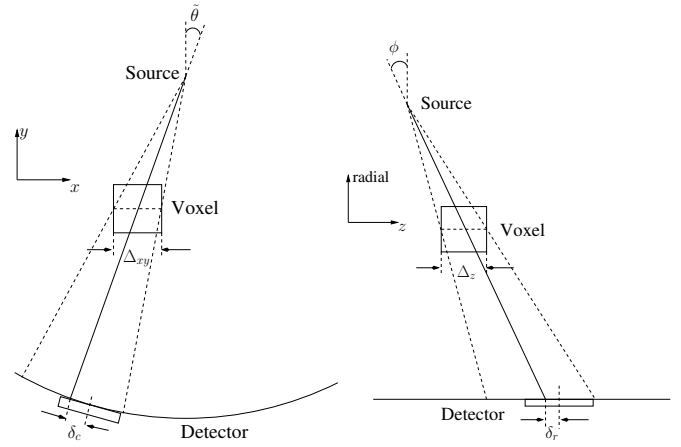

Fig. 1. 3D forward projection geometry used for the distance driven projector.

We studied two different potential functions, given by the l_1 norm prior, which is a special case of generalized Gaussian MRF (GGMRF) [7] when $p = 1$,

$$\rho(\Delta) = |\Delta| \ , \qquad (9)$$

and the q-generalized Gaussian MRF (q-GGMRF) [3].

$$\rho(\Delta) = \frac{|\Delta|^q}{1 + |\Delta/c|^{q-p}} \qquad (10)$$

The q-GGMRF allows more degrees of freedom to control both low-contrast and high-contrast edge characteristics. If $|\Delta| \ll c$, $\rho(\Delta) \approx |\Delta|^q$ and if $|\Delta| \gg c$, $\rho(\Delta) \approx |\Delta/c|^p$ where c is the parameter determining the transition between the two cases. Normally, we will set $q = 2$ and $1 < p < q$. It ensures the overall cost to be convex and, therefore, allows global convergence.

C. Optimization

The overall cost function, obtained by combining the approximate log-likelihood and the prior, is

$$\hat{x} = \arg\min_{x\geq 0}\left\{\frac{1}{2}\|y - Ax\|_D^2 + \sum_{\{s,r\}\in\mathcal{C}} b_{s,r}\rho(x_s - x_r)\right\} \qquad (11)$$

We solve this optimization problem using the iterative coordinate descent (ICD) algorithm [5] in which we scan over all voxels and sequentially optimize each voxel while fixing the others. In order to solve the 1D optimization problem resulting from each pixel update, we design a quadratic substitute functional $q(\Delta;\Delta')$ that upper bounds $\rho(\Delta)$ and optimize the cost with $\rho(\Delta)$ replaced by $q(\Delta;\Delta')$ [8]. In particular,

$$q(\Delta;\Delta') = \frac{\rho'(\Delta')}{2\Delta'}\Delta^2 \qquad (12)$$

where Δ' denotes the voxel difference before this update. In this way, the original 1D line search is converted into a quadratic optimization and the closed form solution can be derived. Since the substitute cost is always an upper bound of the original cost, minimizing the substitute will also produce a
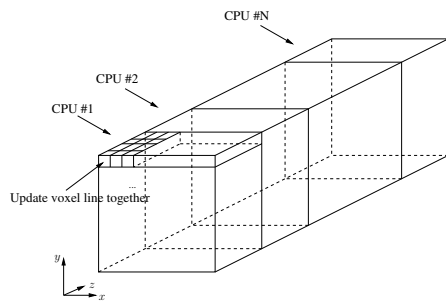
Fig. 2. Parallelized ICD scheme

decreasing sequence of original cost and iterative optimization will lead to the optimal solution of the original problem.

In order to further speed convergence, we also use the non-homogeneous ICD (NHICD) method of [8]. The idea is to focus computation on voxels which tend to generate significant updates. In NHICD, we alternated between a full scan and a partial scan which involves only those voxels which have significant updates at the previous iteration. This scheme provides a further speedup of approximately a factor of three.

D. Parallelization

To utilize multi-core processing and speed up the reconstruction for large image volumes, we implemented a parallelized ICD update scheme. In this scheme, the full image volume is cut into N boxes along the z-direction as shown in Figure 2 and each processor is responsible for updating voxels in one box. Different processors are synchronized once they finish the work; therefore, one synchronization is made per full scan. This will assign each processor a fairly large amount of work to do in parallel and workload is roughly balanced for different processors in order to reduce processor waiting time. Also, since the image is stored with the index in z-direction as the fastest-changing variable, the processors update voxels along z-direction first in order to create better cache efficiency. Moreover, the voxels being updated are selected to be far apart so that they do not share the same sinogram entry, and therefore, can be updated independently.

IV. RESULTS

In this study, we used scan data acquired on a medical scanner and provided by the ALERT (Awareness and Localization of Explosives-Related Threats) Center, at Northeastern University, to conduct our experiments. The reconstructed image is of size $512 \times 512 \times 840$ and the voxel width is 0.975 mm in cross-section in the xy-plane and the slice thickness is 1.25 mm in z-direction. Figure 3 illustrates some of the objects contained in the bag used in our experiment.

Figure 6 demonstrates the quality of different reconstruction algorithms. The FBP reconstruction is blurred, as we can see on the feet of the toy Mr. Potato Head in (a). The shape of some objects are distorted. For example, in the center of (a) and (b), the steel bar, which is of high density and supposed to be a rectangular shape, has been distorted. Also, we can
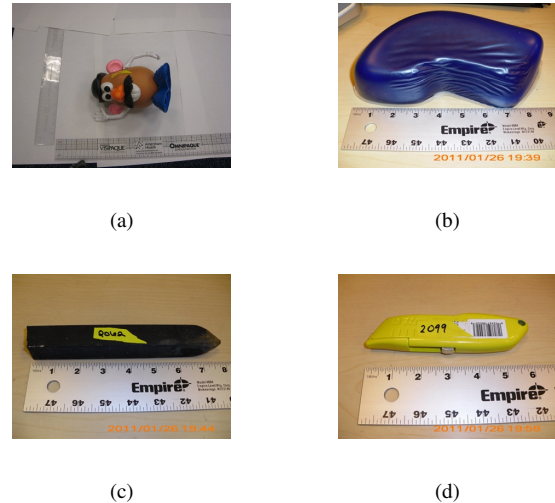

(a)

(b)

(c)

(d)

Fig. 3. Objects contained in the baggage (a) toy Mr. Potato Head (b) gel pad (c) steel bar (d) box cutter

see the severe streaking artifacts, such as the region around the high-density objects in (b). The model-based algorithms, on the other hand, provide better reconstructions. The overall image is sharper and shapes of objects are more accurately recovered. Moreover, the model-based algorithm reduces the structured artifacts as compared to the FBP method. These advantages suggest that the model-based algorithm has the ability to provide more detailed and accurate rendering, which could possibly lead to better detection performance.

We further quantify the reconstruction quality by measuring the noise variance on the uniform region. In Figure 4, a target object, which is a plastic bottle of water, is shown. The streaking artifact caused by the nearby high-density metal object can be easily identified in the FBP reconstruction. In Figure 5, we plot the CT voxel values along the line passing through the bottle of water vertically. We observe that the curve of the FBP reconstruction fluctuates more significantly than the curve of the other two model-based reconstructions. We further calculate the noise variances with different reconstructions along the line and the result is listed in Table I. The FBP reconstruction leads to the largest noise variance, which is the result of the streaking artifacts. It also shows that q-GGMRF gives the smallest noise variance. This is due to the fact that q-GGMRF has more smoothing effects than the l_1 norm prior.

TABLE I
NOISE VARIANCE ON UNIFORM REGION

Method	FBP	l_1 norm prior	q-GGMRF
Noise variance	3042.8	836.0	496.5

V. CONCLUSION

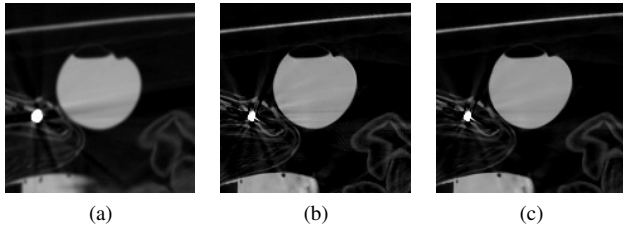In this work, we developed a model-based image reconstruction algorithm and tested it on the data taken from actual

Fig. 4. Reconstructions zoomed to the target area using (a) FBP, (b) l_1 norm prior, and (c) q-GGMRF The round object is the plastic bottle of water.
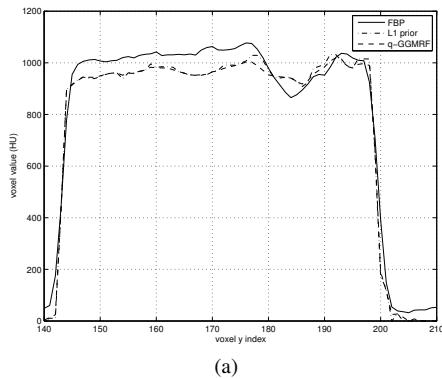

(a)

Fig. 5. CT values for voxels along the line through the center of the target region in Figure 4

baggage. Our algorithm depends on a statistical framework involving a forward model and a prior model. We compared our reconstructions using two different priors, l_1 norm prior and q-GGMRF prior, to the standard FBP algorithm. The model-based algorithms provide better reconstructions and reduce structured artifacts, which suggests potential advantages over the FBP approach.

REFERENCES

[1] R. C. Smith and J. M. Connelly, *Aspects of Explosive Detection*. Elsevier, 2009, ch. 7.

[2] Z. Ying, R. Naidu, and C. Crawford, "Dual energy computed tomography for explosive detection," *J. X-Ray Sci. and Tech.*, vol. 14, no. 4, pp. 235–256, 2006.

[3] J.-B. Thibault, K. Sauer, C. Bouman, and J. Hsieh, "A three-dimensional statistical approach to improved image quality for multi-slice helical CT," *Med. Phys.*, vol. 34, no. 11, pp. 4526–4544, 2007.

[4] S. J. Kisner, E. Haneda, and C. Bouman, "Limited view angle iterative ct reconstruction," in *Proc. SPIE*, vol. 8296, 2012, p. 82960F.

[5] K. Sauer and C. Bouman, "A local update strategy for iterative reconstruction from projections," *IEEE Trans. Signal Process.*, vol. 41, pp. 534–548, Feb. 1993.

[6] B. D. Man and S. Basu, "Distance-driven projection and backprojection in three dimensions," pp. 2463–2475, 2004.

[7] C. Bouman and K. Sauer, "A generalized gaussian image model for edge-preserving MAP estimation," *IEEE Trans. Image Process.*, vol. 2, pp. 296–310, 1993.

[8] Z. Yu, J.-B. Thibault, C. Bouman, K. Sauer, and J. Hsieh, "Fast model-based X-ray CT reconstruction using spatially non-homogeneous icd optimization," *IEEE Trans. Image Process.*, vol. 20, pp. 161–175, Jan. 2011.
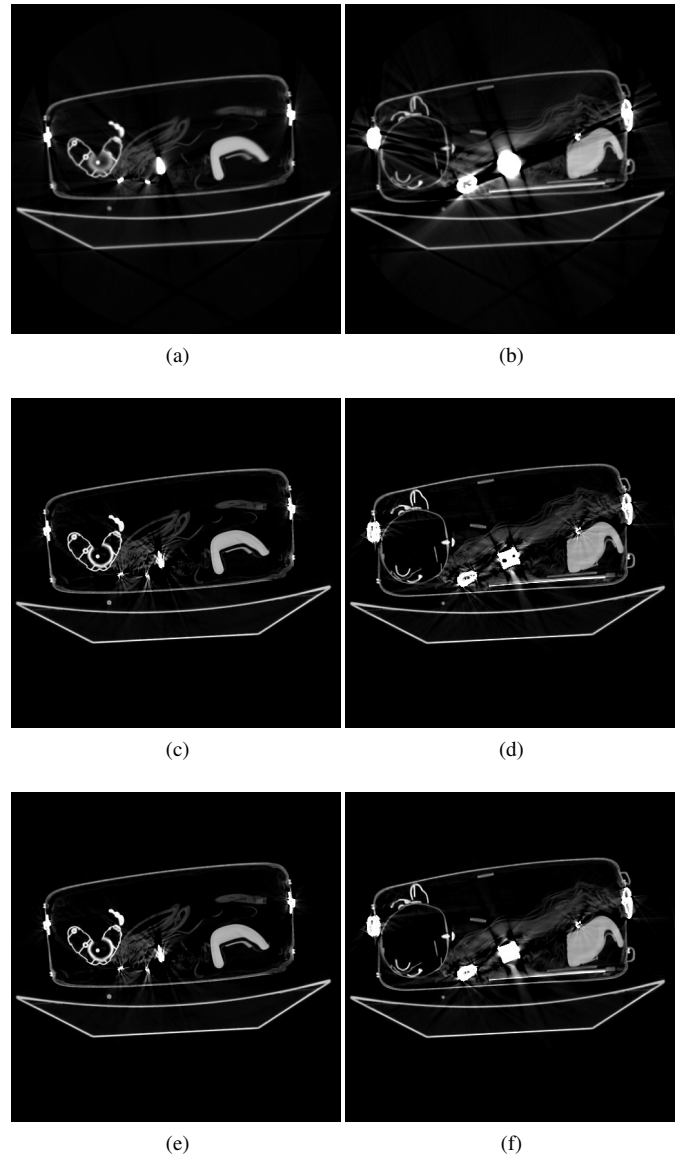
(a)

(b)

(c)

(d)

(e)

(f)

Fig. 6. Reconstruction of the ALERT baggage security data using (a, b) FBP, (c, d) l_1 norm prior, and (e, f) q-GGMRF. The gray scale is in offset Hounsfield Unit (HU), where air $= 0$ HU and the scale range for all results shown is in $[0, 1600]$ HU.